

# TALO: Pushing 3D Vision Foundation Models Towards Globally Consistent Online Reconstruction

Fengyi Zhang<sup>1</sup> Tianjun Zhang<sup>2</sup> Kasma Khosoussi<sup>1</sup> Zheng Zhang<sup>3</sup> Zi Huang<sup>1</sup> Yadan Luo<sup>1</sup>

<sup>1</sup>The University of Queensland <sup>2</sup>Shanghai Jiao Tong University

<sup>3</sup>Harbin Institute of Technology

## Abstract

3D vision foundation models have shown strong generalization in reconstructing key 3D attributes from uncalibrated images through a single feed-forward pass. However, when deployed in online settings such as driving scenarios, predictions are made over temporal windows, making it non-trivial to maintain consistency across time. Recent strategies align consecutive predictions by solving global transformation, yet our analysis reveals their fundamental limitations in assumption validity, local alignment scope, and robustness under noisy geometry. In this work, we propose a higher-DOF and long-term alignment framework based on Thin Plate Spline, leveraging globally propagated control points to correct spatially varying inconsistencies. In addition, we adopt a point-agnostic submap registration design that is inherently robust to noisy geometry predictions. The proposed framework is fully plug-and-play, compatible with diverse 3D foundation models and camera configurations (e.g., monocular or surround-view). Extensive experiments demonstrate that our method consistently yields more coherent geometry and lower trajectory errors across multiple datasets, backbone models, and camera setups, highlighting its robustness and generality. Codes are publicly available at <https://github.com/Xian-Bei/TALO>.

## 1. Introduction

Recent progress in 3D vision foundation models (3DVFM) such as VGGT [38],  $\pi^3$  [42] and MapAnything [12] has redefined the paradigm of 3D reconstruction. These models estimate intrinsics, poses and dense geometry directly from uncalibrated images through a single feed-forward inference, showing strong generalization across diverse scenarios. Nevertheless, most 3DVFM are designed for *offline reconstruction*, where the full sequence is processed at once. When applied to *online settings* such as multi-camera driving scenarios, predictions are made per local window (i.e., submaps), making it non-trivial to maintain consistency across submaps since each is inferred independently.

A common remedy is to align consecutive submaps by solving a *global* transformation between their overlapping regions. VGGT-Long [5] adopts a stable Sim(3) alignment between submaps, which constrains the solution to be 7-DOF to account for rotation, translation, and a global scale. VGGT-SLAM [18] further observes that 3DVFM often produce *inconsistent intrinsics* across submaps, for which a single Sim(3) warp is *insufficient* to successfully align consecutive point clouds. To address this, VGGT-SLAM replaces Sim(3) with a 15-DOF SL(4) warp, improving alignment in controlled indoor datasets. However, our empirical study indicates that SL(4) remains highly unstable and fragile in outdoor multi-camera settings, diverging in over 60% of tested scenes on nuScenes [3] and Waymo [28] across three foundation models [12, 38, 42].

Our analysis identifies three fundamental limitations of these approaches, as illustrated in Fig. 1. The first is their implicit assumption of *globally uniform error fields* that can be corrected by a single linear transformation (see supplementary materials for a formal derivation). Such an assumption is easily violated in realistic outdoor scenarios, especially with multiple cameras and small submap sizes, where geometric distortions *vary spatially*. For example, consecutive submaps may exhibit opposite depth-scale and field-of-view biases across different cameras. In such cases, enforcing a *global* warp, whether Sim(3) or SL(4), inevitably overfits one region at the expense of another, leaving noticeable residuals and compromising trajectory accuracy to compensate for *local* inconsistencies.

Moreover, current pipelines only perform *pairwise alignment* between neighboring submaps, which can only guarantee *short-term optimality*. Before loop closure is triggered, no information from distant submaps is utilized, limiting their ability to achieve global consistency and making them prone to trajectory drift, particularly in long-range sequences. Finally, the under-constrained nature of SL(4) makes it highly sensitive to geometry noise from 3DVFM predictions, often leading to degenerate solutions of implausible poses and divergent scene structures.

These observations motivate our solution **TALO**, a

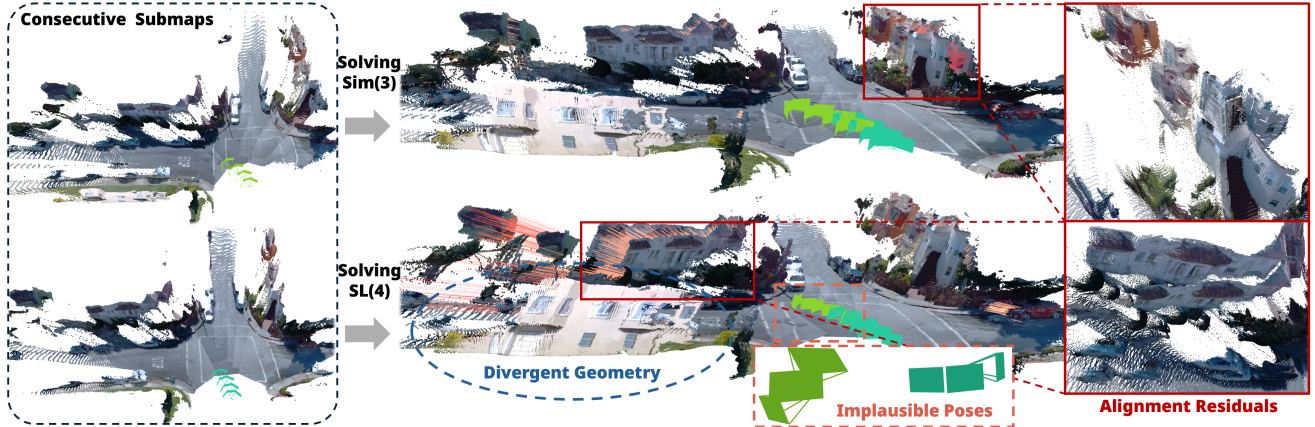


Figure 1. **Degeneration of Sim(3) alignment used in VGGT-Long [5] and SL(4) in VGGT-SLAM [18].** Two consecutive submaps (left) independently predicted by a foundation model exhibit spatially varying, nonlinear geometric inconsistencies. Since neither Sim(3) nor SL(4) can theoretically reconcile such non-global distortions with a single global transformation, enforcing a global warp inevitably overfits one region at the expense of another, leaving noticeable alignment residuals (visualized by **colored connecting lines** and **zoomed-in** on the right, where severe wall ghosting occurs). Moreover, the under-constrained SL(4) is highly sensitive to noise and often yields divergent geometry (e.g., severely tilted buildings, **blue circle**) and physically implausible camera poses. As shown in the **orange box**, the three cameras predicted by the foundation model on the right maintain consistent forward-facing orientations, whereas after SL(4) alignment, their pitch angles diverge drastically, resulting in an impossible trajectory in driving scenarios.

higher-DOF thin-plate alignment framework that is capable of leveraging long-term information to correct spatially varying geometric inconsistencies across submaps in an online manner. In addition, we introduce a point-agnostic submap registration strategy that remains inherently robust to the noisy geometry predicted by 3DVFM.

Specifically, TALO employs a sparse set of 3D control points that are uniformly distributed across the scene to ensure broad spatial coverage. To establish global connections among submaps, these control points are temporally propagated both forward and backward along the sequence, accumulating rich multi-view observations. Each control point aggregates its multi-camera observations through robust fusion to suppress the influence of dynamic objects and outliers, yielding a globally optimal and consistent estimate of its canonical 3D position. Based on these correspondences, Thin Plate Spline (TPS) [1, 6, 34, 44] deformation fields are fitted to warp submaps into a shared canonical configuration, enforcing global geometric consistency. TPS offers flexible, spatially varying correction while regularizing toward local rigidity to preserve structural coherence within each submap. Moreover, we register consecutive submaps by averaging the relative transformations of overlapping frames rather than optimizing over noisy point clouds. This principled, point-agnostic formulation has been extensively validated to produce trajectory estimates that remain robust against geometry noise from 3DVFM. The main contributions of this paper are as follows:

- We provide a systematic analysis of existing 3DVFM alignment strategies, revealing their fundamental limita-

tions in assumption validity, local alignment scope, and robustness under noisy geometry.

- We propose TALO, a higher-DOF and long-term alignment framework based on Thin Plate Spline that leverages global information to correct spatially varying inconsistencies, together with a point-agnostic registration design robust to noisy predictions.
- We deliver a comprehensive, *plug-and-play* system that seamlessly supports any foundation models (e.g., VGGT [38],  $\pi^3$  [42], or MapAnything [12]) and arbitrary camera settings (e.g., monocular or surround-view).
- Extensive experiments demonstrate that TALO consistently produces more coherent geometry and reduced trajectory errors across all foundation models, datasets, and camera setups, highlighting its robustness and generality.

## 2. Related Work

### 2.1. Multi-Stage 3D Reconstruction

Conventional 3D reconstruction pipelines typically begin with Structure-from-Motion (SfM), which recovers sparse geometry and camera intrinsics/extrinsics from image collections. Classical SfM systems [4, 16, 20, 24, 26] generally follow a sequence of stages, including feature extraction, cross-view feature matching, triangulation, and global bundle adjustment. Dense geometry is then reconstructed using Multi-View Stereo (MVS) methods [7, 9, 25, 41], or more recent neural approaches such as Neural Radiance Fields (NeRF) [19, 21, 29, 49] and 3D Gaussian Splatting (3DGS) [11, 13, 46, 47], which typically rely on the sparse structure



and camera poses estimated by SfM. To improve robustness, a number of learning-based approaches have been proposed to replace either individual modules [23, 27, 30, 43] or the entire pipeline [8, 36, 37, 50], making the process differentiable and able to benefit from learned data priors. Nevertheless, these methods remain fundamentally multi-stage and often rely on iterative optimization.

## 2.2. Feed-Forward 3D Reconstruction

A paradigm shift toward end-to-end, feed-forward 3D reconstruction was introduced by DUST3R [40], which predicts dense pointmaps directly from pairs of RGB images, thereby bypassing the traditional multi-stage geometry pipeline. Subsequent works [2, 15, 31, 35, 45, 48] generalize this idea along various directions, including scalability to larger image sets, handling dynamic scenes, and improving geometric accuracy. Moving beyond predicting dense geometry alone, VGGT [38] proposes a unified transformer architecture capable of predicting all core 3D attributes in a single forward pass.  $\pi^3$  [42] further introduces a permutation-equivariant design that removes reference-view bias, while MapAnything [12] extends toward a universal model that supports heterogeneous input-output modality combinations and metric-scale geometry. Together, these feed-forward models unify the prediction of all core 3D attributes within a single network, redefining 3D reconstruction as an end-to-end, single-shot inference problem. We collectively refer to them as *3D Vision Foundation Models (3DVFM)s*.

## 2.3. Online 3D Reconstruction

Feed-forward 3D reconstruction models are generally designed to process two images or an entire sequence at once, requiring additional mechanisms for online reconstruction. Stream3R [14], CUT3R [39], and SLAM3R [17] are built upon DUST3R [40]/MASt3R [15]: Stream3R introduces a causal decoder-only Transformer with KV-cached attention for long-sequence processing; CUT3R maintains a persistent state that continuously updates without restarting inference; and SLAM3R performs local multi-view reconstruction and progressive global registration without explicit pose estimation. StreamVGGT [51], built upon VGGT [38], employs causal attention and token memory for sequential video processing. Beyond architectural extensions, alignment-based methods explicitly address cross-frame consistency and have shown better geometric stability in practice [5]. VGGT-SLAM [18] formulates submap alignment on the  $SL(4)$  manifold, while VGGT-Long [5] adopts low-DOF  $Sim(3)$  alignment for robust long-range reconstruction. Our approach follows this explicit alignment paradigm.

## 3. Method

### 3.1. TALO Overview

To contextualize our framework, we first clarify the notation hierarchy used throughout this paper. A **frame** refers to a synchronized set of **images** captured by different cameras at a single time step  $t$ . A **submap** denotes a short temporal segment composed of several consecutive **frames**. Since our system supports arbitrary  $C$ -camera configurations, all formulations are presented in a generic form applicable to monocular, stereo, and surround-view setups, and the index range  $c \in \{0, \dots, C-1\}$  is omitted for simplicity. We define the first camera ( $c = 0$ ) of each frame as the reference camera.

Given a continuous, synchronized multi-camera video stream  $\{\mathbf{I}^{t,c}\}_{t=0}^{T-1}$ , we segment it into  $K$  submaps  $\{\mathcal{S}_k\}$ , each containing  $O$  overlapping frames with the previous submap and  $L$  newly observed frames ( $O \leq L$ ):

$$\begin{aligned} \mathcal{S}_k &= \mathcal{O}_{k-1,k} \cup \{\mathbf{I}^{t,c}\}_{t=kL}^{(k+1)L-1}, \\ \mathcal{O}_{k-1,k} &= \begin{cases} \{\mathbf{I}^{t,c}\}_{t=kL-O}^{kL-1}, & k > 0, \\ \emptyset, & k = 0. \end{cases} \end{aligned} \quad (1)$$

Each submap is independently processed by a generic 3DFVM  $\mathcal{M}$  to predict per-camera 3D attributes:

$$\mathcal{M}(\mathcal{S}_k) = (\mathbf{K}^{t,c}, \mathbf{T}^{t,c}, \mathbf{P}^{t,c}),$$

where  $\mathbf{K}$ ,  $\mathbf{T}$ , and  $\mathbf{P}$  denote the intrinsic matrix, camera pose, and reconstructed point cloud, respectively. All poses and point clouds are expressed in the coordinate frame of the first camera within the submap.

Our goal is to align all submaps  $\{\mathcal{S}_k\}_{k=0}^{K-1}$  into a globally consistent camera trajectory  $\{\mathbf{T}^{t,c}\}_{t=0}^{T-1}$  and point cloud representation  $\{\mathbf{P}^{t,c}\}_{t=0}^{T-1}$  through an online optimization process based solely on overlapping frames. Our workflow is illustrated in Fig. 2 and detailed in the following subsections: Sect. 3.2 introduces the point-agnostic submap registration; Sect. 3.3 presents the definition and generation of control points; Sect. 3.4 explains the temporal propagation of control points; and Sect. 3.5 introduces the control point aggregation and the TPS deformation field construction to align all submap point clouds into a globally consistent canonical space.

### 3.2. Point-Agnostic Submap Registration

Given two consecutive submaps  $\mathcal{S}_{k-1}$  and  $\mathcal{S}_k$  sharing overlapping frames  $\mathcal{O}_{k-1,k}$ , we estimate a transformation  $\mathbf{H}_{k \rightarrow k-1}$  that maps the coordinate frame of  $\mathcal{S}_k$  to that of  $\mathcal{S}_{k-1}$ . Previous approaches estimate  $\mathbf{H}_{k \rightarrow k-1}$  as a  $Sim(3)$  [5] or  $SL(4)$  [18] transformation that best aligns the predicted point clouds of  $\mathcal{O}_{k-1,k}$  in  $\mathcal{S}_{k-1}$  and  $\mathcal{S}_k$ . However, as analyzed in Sec. 1, such point-based registrations not only

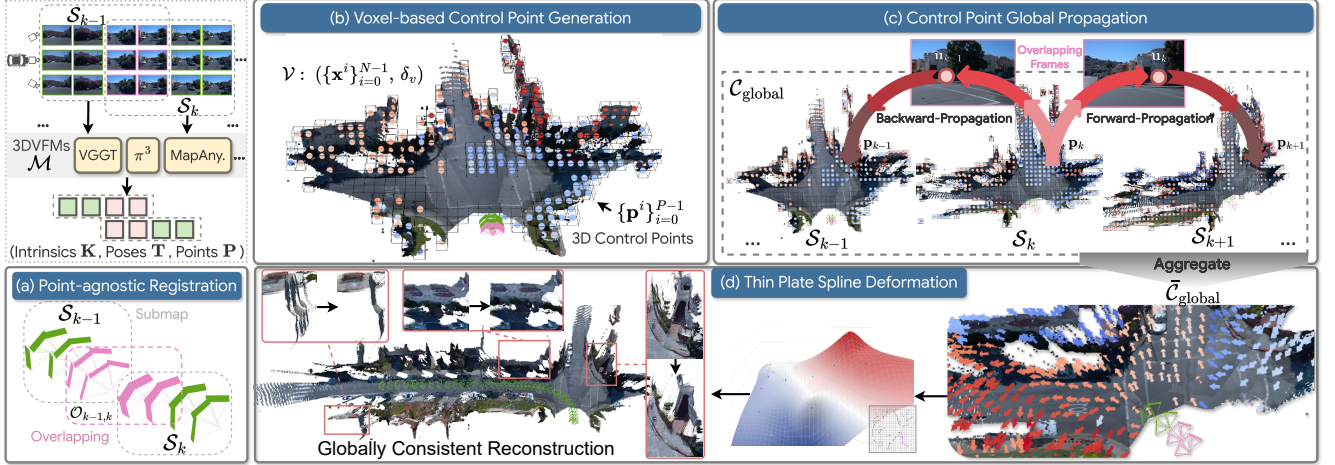


Figure 2. **Workflow of TALO.** TALO processes multi-camera continuous sequences by first dividing them into submaps with overlapping frames. It then performs point-agnostic submap registration by averaging the relative transformations of the overlapping frames, followed by generating control points within the overlapping regions. These control points are globally propagated across submaps, and all their observations are finally aggregated to construct a TPS deformation field that warps every submap into a globally consistent canonical space.

compromise trajectory accuracy to offset local inconsistencies, but are also sensitive to geometry noise in predictions.

In contrast, we estimate  $\mathbf{H}_{k \rightarrow k-1}$  directly from the overlapping camera poses, which are empirically more stable than raw point clouds. Let  $\{\mathbf{T}_{k-1}^i\}_{i=0}^{O-1}$  and  $\{\mathbf{T}_k^i\}_{i=0}^{O-1}$  denote the predicted reference camera poses of  $\mathcal{O}_{k-1,k}$  in  $S_{k-1}$  and  $S_k$ . Although these two pose sets describe the same  $\mathcal{O}$  cameras, they are expressed in distinct local coordinate frames. By aligning them, we bring consecutive submaps into a unified global reference frame (that of  $S_{k-1}$ ). Specifically, for each camera pair  $(\mathbf{T}_{k-1}^i, \mathbf{T}_k^i)$ , we compute the inter-submap transformation as

$$\mathbf{H}_{k \rightarrow k-1}^i = \mathbf{T}_{k-1}^i (\mathbf{T}_k^i)^{-1}, \quad (2)$$

and obtain the final submap transformation  $\mathbf{H}_{k \rightarrow k-1}$  by averaging  $\{\mathbf{H}_{k \rightarrow k-1}^i\}_{i=0}^{O-1}$ . The rotational component is averaged using the Chordal  $L_2$  rotation averaging method, which minimizes the sum of squared Frobenius norm of the difference between each rotation and the estimate [10], while the translational components are averaged.

This minimalistic strategy empirically yields the most stable and accurate trajectory as shown in Sec. 4.2. Through the above procedure, all submaps are sequentially connected and transformed into the coordinate frame of the first image  $\mathbf{I}_{0,0}$ . All poses and points mentioned hereafter are expressed in this unified reference frame.

### 3.3. Control Point Definition and Generation

We define a control point as a fixed spatial location in the underlying 3D world, which ideally remains invariant across all submaps. Formally, let  $\bar{\mathbf{p}}^i$  denote the true world position of the  $i$ -th control point, and let  $\{\mathbf{p}_k^i\}_{k=0}^{K-1}$  denote its predicted observations from  $\mathcal{M}$  in the  $K$  registered submaps. In a globally consistent reconstruction, all

these observations should coincide, *i.e.*,  $\mathbf{p}_k^i = \bar{\mathbf{p}}^i$  for all  $k \in \{0, \dots, K-1\}$  whenever  $\mathbf{p}_k^i$  exists. However, independently inferred submaps inevitably exhibit geometric inconsistencies, causing the same physical location to be reconstructed as different 3D points across submaps. In other words, global control points and their per-submap observations encode the spatial-temporal distortions of geometry. Our goal is therefore to construct a set of global control points  $\mathcal{C}_{\text{global}} = \{\mathbf{p}_k^i \mid k \in \{0, \dots, K-1\}\}_{i=0}^{P-1}$  and their corresponding canonical locations  $\bar{\mathcal{C}}_{\text{global}} = \{\bar{\mathbf{p}}^i\}_{i=0}^{P-1}$ . By aligning  $\mathcal{C}_{\text{global}}$  to  $\bar{\mathcal{C}}_{\text{global}}$ , we explicitly correct these distortions, yielding a globally consistent reconstruction.

To achieve even spatial coverage of control points throughout the 3D scene, we first define a voxel-based control point generation function given a source point set  $\{\mathbf{x}^i \in \mathbb{R}^3\}_{i=0}^{N-1}$  and a voxel size  $\delta_v$ ,

$$\mathcal{V}: (\{\mathbf{x}^i\}_{i=0}^{N-1}, \delta_v) \mapsto \{\mathbf{p}^i\}_{i=0}^{P-1} \subset \{\mathbf{x}^i\}_{i=0}^{N-1}, \quad (3)$$

which voxelizes the input point cloud and selects one representative point per occupied voxel ( $P \ll N$ ). Specifically, we construct a uniform voxel grid in  $\mathbb{R}^3$  with cell size  $\delta_v$ . Let  $\mathbf{m} = \min_i \mathbf{x}^i$  denote the global minimum coordinate. Each input point  $\mathbf{x}^i$  is assigned to a voxel index  $\mathbf{v}^i = \left\lfloor \frac{\mathbf{x}^i - \mathbf{m}}{\delta_v} \right\rfloor \in \mathbb{Z}^3$ , and the geometric center of voxel  $\mathbf{v}$  is  $\mathbf{c}(\mathbf{v}) = \mathbf{m} + (\mathbf{v} + \frac{1}{2}) \delta_v$ . Within each occupied voxel  $\mathbf{v}$ , we select the point closest to its center as its representative:  $i^*(\mathbf{v}) = \arg \min_{i: \mathbf{v}^i = \mathbf{v}} \|\mathbf{x}^i - \mathbf{c}(\mathbf{v})\|_2^2$ . The final control point set is thus obtained as  $\{\mathbf{p}^i\}_{i=0}^{P-1} = \{\mathbf{x}^{i^*(\mathbf{v})} \mid \mathbf{v} \in \mathcal{V}_{\text{occ}}\}$ , where  $\mathcal{V}_{\text{occ}}$  denotes the set of occupied voxels.

### 3.4. Control Point Propagation

Given two consecutive submaps  $\mathcal{S}_{k-1}$  and  $\mathcal{S}_k$  sharing overlapping frames  $\mathcal{O}_{k-1,k}$ , their predicted point clouds of  $\mathcal{O}_{k-1,k}$  are denoted as  $\mathcal{P}_{k-1}^{(k-1) \leftrightarrow k}$  and  $\mathcal{P}_k^{(k-1) \leftrightarrow k}$ , respectively. We first extract a sparse set of control points from  $\mathcal{P}_{k-1}^{(k-1) \leftrightarrow k}$  using the function defined in Eq. (3):

$$\mathcal{C}_{k-1} = \{\mathbf{p}_{k-1}^i\}_{i=0}^{P_{k-1}-1} = \mathcal{V}(\mathcal{P}_{k-1}^{(k-1) \leftrightarrow k}, \delta_v). \quad (4)$$

For clarity, we describe the subsequent process using a single control point  $\mathbf{p}_{k-1} \in \mathcal{C}_{k-1}$  and omit the superscript  $i$ . Owing to the pixel-aligned nature of foundation models, each 3D point  $\mathbf{p}_{k-1} \in \mathcal{P}_{k-1}^{(k-1) \leftrightarrow k}$  inherently originates from a pixel  $\mathbf{u}_{k-1}$  in an overlapping image  $\mathbf{I} \in \mathcal{O}_{k-1,k}$ . Since  $\mathbf{I} \in \mathcal{O}_{k-1,k} \subset \mathcal{S}_k$ , we can unproject the same pixel  $\mathbf{u}_{k-1}$  into a 3D position  $\mathbf{p}_k \in \mathcal{P}_k^{(k-1) \leftrightarrow k}$  using the camera parameters of  $\mathcal{S}_k$ . This establishes a control-point correspondence between two consecutive submaps representing the same physical location bridged by overlapping frames.

To achieve global consistency beyond short-term optimality, we further propagate control points across the entire sequence. Specifically, we illustrate how to propagate the control point  $\mathbf{p}_k$  of  $\mathcal{S}_k$ , originally generated from  $\mathcal{S}_{k-1}$ , to the next submap  $\mathcal{S}_{k+1}$ , which shares the overlapping frames  $\mathcal{O}_{k,k+1}$  with  $\mathcal{S}_k$ . We first project  $\mathbf{p}_k \in \mathcal{P}_k^{(k-1) \leftrightarrow k}$  onto an image in  $\mathcal{O}_{k,k+1}$ , obtaining its pixel location  $\mathbf{u}_k$ . In practice, it may project onto multiple images within  $\mathcal{O}_{k,k+1}$ ; we retain the one with the smallest reprojection error. Since  $\mathcal{O}_{k,k+1} \subset \mathcal{S}_{k+1}$ , we unproject the same pixel  $\mathbf{u}_{k+1} = \mathbf{u}_k$  into 3D position  $\mathbf{p}_{k+1} \in \mathcal{P}_{k+1}^{k \leftrightarrow k+1}$ . Repeating this process forms a rich observation sequence for the same world location. If a control point fails to obtain a valid projection in any submap, its propagation is terminated.

In implementation, when performing voxelization for new control-point generation (Eq. (4)) in a new submap  $\mathcal{S}_k$ , control points from the previous submap  $\mathcal{S}_{k-1}$  are first propagated forward to  $\mathcal{S}_k$ . A new control point is instantiated only if its voxel is not already occupied by any propagated control point from  $\mathcal{S}_{k-1}$ . Conversely, each newly created control point is back-propagated to  $\mathcal{S}_{k-1}$  to enrich mutual observations between the two submaps. All control point observations are maintained in a global pool  $\mathcal{C}_{\text{global}} = \{\mathbf{p}_k^i \mid k \in \{0, \dots, K-1\}\}_{i=0}^{P-1}$ , forming a globally connected control-point graph that serves as the foundation for the subsequent TPS alignment.

### 3.5. Thin Plate Spline Deformation

Given the global control point observations  $\mathcal{C}_{\text{global}} = \{\mathbf{p}_k^i \mid k \in \{0, \dots, K-1\}\}_{i=0}^{P-1}$ , we first define the canonical 3D position of the  $i$ -th control point by robustly aggregating these multi-submap observations:

$$\bar{\mathbf{p}}^i = \text{Aggregate}(\{\mathbf{p}_k^i \mid k \in \{0, \dots, K-1\}\}), \quad (5)$$

where the aggregation is implemented as a MAD-filtered mean to suppress the influence of dynamic objects and outliers. Before TPS fitting, we apply a local Gaussian smoothing to the displacement vectors  $\Delta_k^i = \bar{\mathbf{p}}^i - \mathbf{p}_k^i$ . For each point  $\mathbf{p}_k^i$ , we find its  $Q$  nearest neighbors  $\mathcal{N}_Q(i)$  based on Euclidean distance  $d_{ij} = \|\mathbf{p}_k^i - \mathbf{p}_k^j\|_2$ , and compute a Gaussian-weighted average of neighbor displacements:

$$\tilde{w}_{ij} = \exp\left(-\frac{d_{ij}^2}{2\sigma^2}\right), \quad w_{ij} = \frac{\tilde{w}_{ij}}{\sum_{l \in \mathcal{N}_Q(i)} \tilde{w}_{il}}.$$

The smoothed displacement is then given by

$$\Delta_k^{i, \text{sm}} = \sum_{j \in \mathcal{N}_Q(i)} w_{ij} \Delta_k^j, \quad \bar{\mathbf{p}}_k^i \leftarrow \mathbf{p}_k^i + \Delta_k^{i, \text{sm}}.$$

The bandwidth  $\sigma$  is automatically estimated as the median distance to the  $K$ -th nearest neighbor, ensuring scale adaptivity to local point density. This Gaussian filtering enforces local spatial coherence in both the magnitude and direction of corrections, effectively reducing noise and stabilizing the subsequent TPS deformation.

We then employ a 3D Thin Plate Spline (TPS) [1, 6, 34, 44] deformation  $\mathcal{F}_k : \mathbb{R}^3 \rightarrow \mathbb{R}^3$ , a classical kernel-based mapping that minimizes bending energy while interpolating given correspondences. TPS provides a continuous spatial transformation that preserves global smoothness and local rigidity, making it well-suited for correcting local geometric distortions in our setting. Let  $\mathcal{C}_k = \{\mathbf{p}_k^i\}_{i=0}^{P_k-1}$  denotes all control points that are observed in  $\mathcal{S}_k$  and  $\bar{\mathcal{C}}_k = \{\bar{\mathbf{p}}^i\}_{i=0}^{P-1}$  their corresponding canonical positions, the TPS deformation of  $\mathcal{S}_k$  is parameterized as

$$\mathcal{F}_k(\mathbf{x}) = A_k \mathbf{x} + \mathbf{b}_k + \sum_{i=1}^{P_k} \mathbf{w}_k^i \phi(\|\mathbf{x} - \mathbf{p}_k^i\|), \quad (6)$$

where  $\mathbf{x} \in \mathbb{R}^3$  denotes any spatial position,  $A_k \in \mathbb{R}^{3 \times 3}$  and  $\mathbf{b}_k \in \mathbb{R}^3$  model the global affine component,  $\mathbf{w}_k^i \in \mathbb{R}^3$  are the TPS kernel weights associated with control points  $\{\mathbf{p}_k^i\}$ , and  $\phi(r)$  is a radial basis kernel that defines the non-rigid influence of each  $\mathbf{p}_k^i$ , which is set to  $\phi(r) = r$  following the standard biharmonic radial basis in 3D. The parameters  $\{A_k, \mathbf{b}_k, \mathbf{w}_k^i\}$  are estimated by minimizing the energy:

$$\min_{A_k, \mathbf{b}_k, \mathbf{w}_k} \sum_i^{P_k} \|\mathcal{F}_k(\mathbf{p}_k^i) - \bar{\mathbf{p}}^i\|^2 + \lambda \text{tr}(\mathbf{w}_k^\top K_k \mathbf{w}_k), \quad (7)$$

where  $(K_k)_{ij} = \phi(\|\mathbf{p}_k^i - \mathbf{p}_k^j\|)$  encodes pairwise radial interactions among control points, and  $\lambda$  controls the smoothness regularization (bending energy). This closed-form solution yields a smooth, differentiable deformation  $\mathcal{F}_k$  that aligns the submap  $\mathcal{S}_k$  to the global geometric consensus by interpolating the control-point correspondences and smoothly deforming the remaining points. Applying  $\mathcal{F}_k$  to all points within  $\mathcal{S}_k$  produces a locally consistent, globally coherent alignment across all submaps.



Table 1. Camera trajectory accuracy on **Waymo** [28], reported as ATE (RMSE [m]), RTE (RMSE [m]), and RRE (RMSE [ $^{\circ}$ ]). Best results under each foundation model are **bold underlined**, and **catastrophic failures** (ATE RMSE > 5% of GT trajectory length) are in red.

Foundation Model	Alignment Strategy	163453191685903.			183829460855609.			315615587265462.			346181117917711.			405841035328651.			520018670674820.			610454533463565.			Avg.		
		ATE $^{\downarrow}$	RTE $^{\downarrow}$	RRE $^{\downarrow}$	ATE $^{\downarrow}$	RTE $^{\downarrow}$	RRE $^{\downarrow}$	ATE $^{\downarrow}$	RTE $^{\downarrow}$	RRE $^{\downarrow}$	ATE $^{\downarrow}$	RTE $^{\downarrow}$	RRE $^{\downarrow}$	ATE $^{\downarrow}$	RTE $^{\downarrow}$	RRE $^{\downarrow}$	ATE $^{\downarrow}$	RTE $^{\downarrow}$	RRE $^{\downarrow}$	ATE $^{\downarrow}$	RTE $^{\downarrow}$	RRE $^{\downarrow}$	ATE $^{\downarrow}$	RTE $^{\downarrow}$	RRE $^{\downarrow}$
VGGT [38]	VGGT-Long [5]	1.85	0.36	0.54	0.28	0.20	0.50	1.59	0.38	0.78	<b>1.45</b>	<b>0.40</b>	0.89	1.41	0.31	0.66	2.76	<b>0.38</b>	1.07	0.55	0.24	0.56	1.42	0.32	0.71
	VGGT-SLAM [18]	<b>12.45</b>	<b>4.16</b>	<b>4.39</b>	1.04	0.97	3.84	<b>13.18</b>	<b>4.01</b>	<b>4.79</b>	<b>16.35</b>	<b>11.16</b>	<b>17.32</b>	<b>7.04</b>	<b>3.88</b>	<b>10.36</b>	<b>34.75</b>	<b>13.72</b>	<b>31.05</b>	0.64	0.60	4.58	12.21	5.50	10.90
	TALO	<b>1.37</b>	<b>0.32</b>	<b>0.15</b>	<b>0.10</b>	<b>0.07</b>	<b>0.08</b>	<b>0.63</b>	<b>0.23</b>	<b>0.13</b>	2.30	0.68	<b>0.14</b>	<b>0.91</b>	<b>0.19</b>	<b>0.13</b>	<b>2.21</b>	0.40	<b>0.25</b>	<b>0.10</b>	<b>0.07</b>	<b>0.08</b>	<b>1.09</b>	<b>0.28</b>	<b>0.14</b>
$\pi^3$ [42]	VGGT-Long [5]	<b>0.95</b>	0.30	0.71	0.61	0.29	0.84	1.69	0.71	1.25	7.91	0.96	1.06	1.05	0.33	0.81	2.98	0.48	1.37	0.37	0.26	0.48	2.22	0.48	0.93
	VGGT-SLAM [18]	<b>19.56</b>	<b>6.52</b>	<b>4.78</b>	1.03	0.59	4.47	<b>29.85</b>	<b>9.49</b>	<b>6.87</b>	<b>65.73</b>	<b>13.29</b>	<b>8.58</b>	2.00	1.98	7.42	<b>35.84</b>	<b>6.94</b>	<b>30.46</b>	1.59	0.67	6.16	22.23	5.64	9.82
	TALO	0.97	<b>0.23</b>	<b>0.31</b>	<b>0.15</b>	<b>0.10</b>	<b>0.22</b>	<b>1.29</b>	<b>0.40</b>	<b>0.28</b>	<b>2.02</b>	<b>0.52</b>	<b>0.17</b>	<b>0.24</b>	<b>0.09</b>	<b>0.15</b>	<b>1.03</b>	<b>0.36</b>	<b>0.45</b>	<b>0.31</b>	<b>0.14</b>	<b>0.10</b>	<b>0.86</b>	<b>0.26</b>	<b>0.24</b>
Map. [12]	VGGT-Long [5]	2.71	0.37	1.61	0.40	0.21	0.43	<b>10.60</b>	<b>0.99</b>	<b>3.34</b>	7.26	0.87	1.33	1.16	0.33	1.17	<b>3.05</b>	1.30	2.89	0.61	0.36	1.19	3.68	0.63	1.71
	VGGT-SLAM [18]	<b>46.17</b>	<b>7.09</b>	<b>29.35</b>	4.62	2.93	6.03	<b>48.03</b>	<b>5.27</b>	<b>31.08</b>	<b>96.80</b>	<b>50.48</b>	<b>41.68</b>	<b>6.25</b>	<b>2.87</b>	<b>14.36</b>	<b>10.46</b>	<b>8.35</b>	<b>38.96</b>	1.16	1.22	3.56	30.50	11.17	23.57
	TALO	<b>1.55</b>	<b>0.28</b>	<b>0.96</b>	<b>0.21</b>	<b>0.12</b>	<b>0.15</b>	<b>0.72</b>	<b>0.46</b>	<b>0.27</b>	<b>1.62</b>	<b>0.64</b>	<b>0.26</b>	<b>0.56</b>	<b>0.27</b>	<b>0.52</b>	5.00	<b>1.01</b>	<b>1.86</b>	<b>0.18</b>	<b>0.19</b>	<b>0.20</b>	<b>1.40</b>	<b>0.42</b>	<b>0.60</b>

Table 2. Camera trajectory accuracy on **nuScenes** [3], reported as ATE (RMSE [m]), RTE (RMSE [m]), and RRE (RMSE [ $^{\circ}$ ]). Best results under each foundation model are **bold underlined**, and **catastrophic failures** (ATE RMSE > 5% of GT trajectory length) are in red.

Foundation Model	Alignment Strategy	scene-0003			scene-0012			scene-0013			scene-0036			scene-0039			scene-0092			scene-0094			Avg.		
		ATE $^{\downarrow}$	RTE $^{\downarrow}$	RRE $^{\downarrow}$	ATE $^{\downarrow}$	RTE $^{\downarrow}$	RRE $^{\downarrow}$	ATE $^{\downarrow}$	RTE $^{\downarrow}$	RRE $^{\downarrow}$	ATE $^{\downarrow}$	RTE $^{\downarrow}$	RRE $^{\downarrow}$	ATE $^{\downarrow}$	RTE $^{\downarrow}$	RRE $^{\downarrow}$	ATE $^{\downarrow}$	RTE $^{\downarrow}$	RRE $^{\downarrow}$	ATE $^{\downarrow}$	RTE $^{\downarrow}$	RRE $^{\downarrow}$	ATE $^{\downarrow}$	RTE $^{\downarrow}$	RRE $^{\downarrow}$
VGGT [38]	VGGT-Long [5]	0.31	0.18	0.40	1.61	0.48	0.80	1.37	0.43	0.63	2.52	0.63	0.62	<b>1.45</b>	<b>0.44</b>	0.70	3.02	0.65	0.44	<b>1.15</b>	0.48	0.47	1.63	0.47	0.58
	VGGT-SLAM [18]	<b>0.19</b>	0.24	1.57	<b>19.58</b>	<b>4.24</b>	<b>3.48</b>	<b>11.58</b>	<b>2.74</b>	<b>5.56</b>	<b>21.09</b>	<b>4.66</b>	<b>3.35</b>	<b>28.42</b>	<b>4.73</b>	<b>1.67</b>	<b>11.02</b>	<b>2.06</b>	<b>0.98</b>	<b>30.83</b>	<b>4.08</b>	<b>28.93</b>	17.53	3.25	6.51
	TALO	0.36	<b>0.13</b>	<b>0.20</b>	<b>1.11</b>	<b>0.40</b>	<b>0.35</b>	<b>0.71</b>	<b>0.31</b>	<b>0.17</b>	<b>1.05</b>	<b>0.40</b>	<b>0.18</b>	1.75	0.48	<b>0.20</b>	<b>3.01</b>	<b>0.61</b>	<b>0.14</b>	1.17	<b>0.29</b>	<b>0.11</b>	<b>1.31</b>	<b>0.37</b>	<b>0.19</b>
$\pi^3$ [42]	VGGT-Long [5]	0.49	0.31	0.99	2.26	0.66	1.40	<b>1.60</b>	1.07	4.47	2.20	0.42	0.73	1.57	<b>0.32</b>	0.97	1.17	0.49	0.75	2.16	0.96	1.09	1.63	0.60	1.49
	VGGT-SLAM [18]	0.42	0.37	2.46	8.14	6.34	12.75	<b>12.85</b>	<b>3.83</b>	<b>11.25</b>	7.89	8.02	12.19	<b>25.37</b>	<b>6.38</b>	<b>10.04</b>	2.52	4.01	4.99	<b>8.39</b>	<b>2.46</b>	<b>1.86</b>	9.37	4.49	7.93
	TALO	<b>0.31</b>	<b>0.17</b>	<b>0.34</b>	<b>1.08</b>	<b>0.43</b>	<b>0.46</b>	1.85	<b>0.86</b>	<b>0.78</b>	<b>1.34</b>	<b>0.39</b>	<b>0.24</b>	<b>1.30</b>	0.36	<b>0.19</b>	<b>0.61</b>	<b>0.32</b>	<b>0.35</b>	<b>0.63</b>	<b>0.32</b>	<b>0.30</b>	<b>1.02</b>	<b>0.41</b>	<b>0.38</b>
Map. [12]	VGGT-Long [5]	0.34	0.21	0.43	1.76	0.48	1.25	1.79	0.38	1.35	4.58	0.52	1.48	3.36	0.68	1.97	1.72	1.10	1.23	2.80	0.61	1.64	2.34	0.57	1.34
	VGGT-SLAM [18]	1.12	0.46	6.71	<b>53.69</b>	<b>6.45</b>	<b>33.69</b>	<b>21.76</b>	<b>3.74</b>	<b>11.96</b>	<b>38.99</b>	<b>12.24</b>	<b>42.71</b>	<b>50.34</b>	<b>24.39</b>	<b>19.34</b>	6.81	2.51	5.24	4.31	1.98	5.25	25.29	7.40	17.84
	TALO	<b>0.21</b>	<b>0.14</b>	<b>0.23</b>	<b>0.75</b>	<b>0.36</b>	<b>0.44</b>	<b>0.46</b>	<b>0.33</b>	<b>0.28</b>	<b>1.25</b>	<b>0.51</b>	<b>0.28</b>	<b>1.91</b>	<b>0.61</b>	<b>0.28</b>	<b>0.89</b>	<b>0.62</b>	<b>0.26</b>	<b>0.89</b>	<b>0.40</b>	<b>0.19</b>	<b>0.91</b>	<b>0.42</b>	<b>0.28</b>

## 4. Experiments

### 4.1. Experimental Setup

**Datasets.** We conduct experiments on two multi-camera outdoor datasets: Waymo [28] with 5 cameras and nuScenes [3] with 6 cameras. Images are synchronized at 2 Hz and downsampled following the default settings of each foundation model, and LiDAR scans are accumulated as the same Hz as ground-truth for dense 3D reconstruction evaluation. Sky pixels are removed using a dedicated sky-segmentation model to avoid depth ambiguity.

**Metrics.** Following common practices, we evaluate trajectories using Absolute Trajectory Error (ATE RMSE), Relative Translation Error (RTE RMSE), and Relative Rotation Error (RRE RMSE), while evaluating 3D reconstruction quality using Accuracy, Completeness, and Chamfer Distance. Predicted camera poses are aligned to the ground truth using the Umeyama algorithm [33], and the same transformation is applied to the reconstructed point clouds.

**Baselines.** We primarily compare against VGGT-SLAM [18] and VGGT-Long [5], two recent systems that also align consecutive outputs of 3D foundation models for incremental reconstruction. Since both systems are designed exclusively for monocular video and employ only VGGT [38] as the backbone, we re-implemented them using their official code within a unified framework, with identical back-end optimization, loop-closure mechanisms (both from VGGT-SLAM [18]), and experiment settings, while extending the pipeline to support multi-camera sequences and additional foundation models including  $\pi^3$  [42] and MapAnything [12]. This setup enables a clean

and controlled study of alignment behavior across different datasets and foundation backbones.

**Implementation Details.** All experiments are conducted on a single NVIDIA RTX 6000 Ada (48 GB) GPU. During optimization and evaluation, we retain only points whose prediction confidence is above the 60<sup>th</sup> percentile. The voxel resolution  $\delta_v$  for control-point generation is set to 5% of the current submap’s point-cloud radius, while the neighborhood size for control-point filtering is fixed to  $Q = 32$ . The submap length is set to  $L = 2$  to achieve a more responsive online reconstruction (i.e., one update per second under the current 2 Hz frame rate). The number of overlapping frames is simply set to  $O = L$ . Additional results with different submap sizes are presented in the ablation study. For models such as VGGT [38] and  $\pi^3$  [42] which lack metric-scale, we estimate a global scale factor before control-point propagation to avoid using high-DOF TPS for global scale correction. For models like MapAnything [12] which maintain metric scale prediction, this step is omitted, and we also disable scale estimation in VGGT-Long’s [5] Sim(3) alignment for fairness, whereas in VGGT-SLAM [18] (SL(4) formulation) the scale cannot be explicitly decoupled.

### 4.2. Trajectory Evaluation

We evaluate camera trajectory accuracy on Waymo [28] and nuScenes [3] using all cameras, as summarized in Table 1 and Table 2. Our proposed TALO achieves the best results across all datasets and backbones, **with zero failure cases**. The average ATE remains consistently around  $\sim 1$  m on both datasets for all tested backbones. More importantly, rotational accuracy improves substantially. For instance, on Waymo, our method reduces RRE from 0.71 $^{\circ}$  (VGGT-

Table 3. Reconstructed geometry evaluation on the **Waymo** [28] dataset, reported as Accuracy, Completeness, and Chamfer Distance.

Foundation Model	Alignment Strategy	163453191685903.			183829460855609.			315615587265462.			346181117917711.			405841035328651.			520018670674820.			610454533463565.			Avg.		
		Acc. $\downarrow$	Com. $\downarrow$	Cha. $\downarrow$	Acc. $\downarrow$	Com. $\downarrow$	Cha. $\downarrow$	Acc. $\downarrow$	Com. $\downarrow$	Cha. $\downarrow$	Acc. $\downarrow$	Com. $\downarrow$	Cha. $\downarrow$	Acc. $\downarrow$	Com. $\downarrow$	Cha. $\downarrow$	Acc. $\downarrow$	Com. $\downarrow$	Cha. $\downarrow$	Acc. $\downarrow$	Com. $\downarrow$	Cha. $\downarrow$	Acc. $\downarrow$	Com. $\downarrow$	Cha. $\downarrow$
VGGT [38]	VGGT-Long [5]	0.62	0.84	0.73	0.26	<b>0.71</b>	<b>0.49</b>	0.76	0.78	0.77	0.85	1.40	1.13	0.55	0.80	0.68	0.89	<b>0.99</b>	0.94	0.56	0.48	0.52	0.64	0.86	0.75
	VGGT-SLAM [18]	3.87	6.50	5.18	5.04	6.44	5.74	9.06	8.67	8.87	9.46	9.39	9.43	7.37	8.24	7.80	5.22	9.24	7.23	5.12	3.66	4.39	6.45	7.45	6.95
	TALO	<b>0.46</b>	<b>0.58</b>	<b>0.52</b>	<b>0.18</b>	0.82	0.50	<b>0.48</b>	<b>0.63</b>	<b>0.56</b>	<b>0.61</b>	<b>1.28</b>	<b>0.94</b>	<b>0.37</b>	<b>0.68</b>	<b>0.52</b>	<b>0.74</b>	<b>0.90</b>	<b>0.35</b>	<b>0.40</b>	<b>0.37</b>	<b>0.45</b>	<b>0.78</b>	<b>0.62</b>	<b>0.62</b>
$\pi^3$ [42]	VGGT-Long [5]	0.39	<b>0.50</b>	0.45	0.41	0.67	0.54	0.86	1.15	1.00	1.32	2.00	1.66	0.41	0.53	0.47	1.15	1.11	1.13	0.49	0.34	0.42	0.72	0.90	0.81
	VGGT-SLAM [18]	8.51	9.14	8.82	2.77	3.24	3.01	8.63	9.49	9.06	9.53	9.63	9.58	3.07	3.41	3.24	1.68	7.79	4.73	0.96	1.16	1.06	5.02	6.27	5.64
	TALO	<b>0.37</b>	<b>0.50</b>	<b>0.43</b>	<b>0.18</b>	<b>0.56</b>	<b>0.37</b>	<b>0.67</b>	<b>0.87</b>	<b>0.77</b>	<b>1.21</b>	<b>1.42</b>	<b>1.31</b>	<b>0.18</b>	<b>0.41</b>	<b>0.30</b>	<b>0.60</b>	<b>0.63</b>	<b>0.61</b>	<b>0.32</b>	<b>0.31</b>	<b>0.31</b>	<b>0.50</b>	<b>0.67</b>	<b>0.59</b>
Map. [12]	VGGT-Long [5]	1.23	1.23	1.23	0.41	0.62	0.51	1.86	1.52	1.69	1.98	1.82	1.90	0.68	1.09	0.88	<b>2.73</b>	1.12	<b>1.92</b>	<b>0.85</b>	0.62	0.73	1.39	1.15	1.27
	VGGT-SLAM [18]	1.66	9.36	5.51	2.38	4.74	3.56	2.28	9.32	5.80	4.97	9.54	7.26	7.69	7.87	7.78	9.37	6.80	8.08	6.20	7.07	6.63	4.93	7.81	6.37
	TALO	<b>1.10</b>	<b>1.14</b>	<b>1.12</b>	<b>0.38</b>	<b>0.59</b>	<b>0.49</b>	<b>1.09</b>	<b>0.76</b>	<b>0.92</b>	<b>1.65</b>	<b>1.42</b>	<b>1.54</b>	<b>0.51</b>	<b>0.92</b>	<b>0.72</b>	3.04	<b>0.93</b>	1.99	0.86	<b>0.58</b>	<b>0.72</b>	<b>1.23</b>	<b>0.90</b>	<b>1.07</b>

Table 4. Reconstructed geometry evaluation on the **nuScenes** [3] dataset, reported as Accuracy, Completeness, and Chamfer Distance.

Foundation Model	Alignment Strategy	scene-0003			scene-0012			scene-0013			scene-0036			scene-0039			scene-0092			scene-0094			Avg.		
		Acc. $\downarrow$	Com. $\downarrow$	Cha. $\downarrow$	Acc. $\downarrow$	Com. $\downarrow$	Cha. $\downarrow$	Acc. $\downarrow$	Com. $\downarrow$	Cha. $\downarrow$	Acc. $\downarrow$	Com. $\downarrow$	Cha. $\downarrow$	Acc. $\downarrow$	Com. $\downarrow$	Cha. $\downarrow$	Acc. $\downarrow$	Com. $\downarrow$	Cha. $\downarrow$	Acc. $\downarrow$	Com. $\downarrow$	Cha. $\downarrow$	Acc. $\downarrow$	Com. $\downarrow$	Cha. $\downarrow$
VGGT [38]	VGGT-Long [5]	<b>0.38</b>	<b>1.15</b>	<b>0.76</b>	0.58	<b>1.01</b>	<b>0.79</b>	1.02	1.03	1.02	1.39	<b>1.66</b>	<b>1.54</b>	1.35	1.70	1.52	1.12	<b>0.84</b>	0.98	<b>1.53</b>	<b>0.58</b>	<b>1.06</b>	1.05	<b>1.14</b>	<b>1.09</b>
	VGGT-SLAM [18]	0.97	1.76	1.36	8.49	7.39	7.94	5.48	6.17	5.82	8.88	8.98	8.93	7.52	7.25	7.38	4.58	5.51	5.05	3.46	1.53	2.50	5.63	5.51	5.57
	TALO	0.49	1.40	0.94	<b>0.57</b>	1.10	0.83	<b>0.85</b>	<b>0.90</b>	<b>0.88</b>	<b>1.36</b>	1.72	<b>1.54</b>	<b>1.18</b>	<b>1.59</b>	<b>1.38</b>	<b>1.00</b>	0.86	<b>0.93</b>	1.74	0.80	1.27	<b>1.03</b>	1.19	1.11
$\pi^3$ [42]	VGGT-Long [5]	<b>0.24</b>	<b>1.24</b>	<b>0.74</b>	<b>0.43</b>	1.10	0.76	1.04	<b>1.40</b>	1.22	<b>1.62</b>	<b>2.43</b>	<b>2.03</b>	1.60	2.17	1.88	<b>0.60</b>	<b>0.67</b>	<b>0.63</b>	1.26	1.35	1.30	0.97	1.48	1.22
	VGGT-SLAM [18]	1.10	1.81	1.46	6.66	7.79	7.22	4.15	3.84	4.00	9.28	9.25	9.26	9.19	9.26	9.23	8.66	8.30	8.48	2.85	2.34	2.59	5.98	6.08	6.03
	TALO	0.27	1.31	0.79	0.44	<b>0.99</b>	<b>0.72</b>	<b>0.94</b>	<b>1.40</b>	<b>1.17</b>	1.67	2.47	2.07	<b>1.50</b>	<b>1.98</b>	<b>1.74</b>	0.66	0.75	0.71	<b>0.90</b>	<b>1.07</b>	<b>0.98</b>	<b>0.91</b>	<b>1.42</b>	<b>1.17</b>
Map. [12]	VGGT-Long [5]	0.52	<b>1.41</b>	0.97	0.87	<b>0.99</b>	0.93	0.79	1.43	1.11	1.54	1.98	1.76	1.33	2.45	1.89	1.47	0.59	1.03	2.07	0.87	1.47	1.23	1.39	1.31
	VGGT-SLAM [18]	0.46	1.15	0.80	0.65	9.41	5.03	4.57	7.64	6.10	9.20	9.44	9.32	6.91	8.98	7.94	7.13	2.45	4.79	7.31	5.30	6.31	5.18	6.34	5.76
	TALO	<b>0.48</b>	1.44	<b>0.96</b>	<b>0.83</b>	<b>0.99</b>	<b>0.91</b>	<b>0.61</b>	<b>1.10</b>	<b>0.86</b>	<b>1.35</b>	<b>1.57</b>	<b>1.46</b>	<b>1.10</b>	<b>1.65</b>	<b>1.38</b>	<b>1.63</b>	<b>0.33</b>	<b>0.98</b>	<b>1.78</b>	<b>0.51</b>	<b>1.15</b>	<b>1.11</b>	<b>1.09</b>	<b>1.10</b>

Long [5]) to only 0.14°, achieving nearly a  $5\times$  improvement. As shown in Fig. 3, RRE better reflects trajectory deviation than ATE. In the two visualized examples, VGGT-Long produces trajectories with noticeable directional drift, despite similar ATE values, while our TALO preserves the correct orientation, leading to much lower RRE.

In contrast, the SL(4) alignment used in VGGT-SLAM [18] exhibits extreme instability in such outdoor, long-trajectory scenarios with small submap sizes, failing in over 60% of the tested sequences. Most failures are caused by divergence or collapse, as illustrated in Fig. 3. This instability arises from its excessive projective degrees of freedom, which allow highly distorted and even implausible transformations; once such a transformation occurs, it propagates to subsequent submaps, corrupting the entire trajectory. The Sim(3) alignment in VGGT-Long [5] demonstrates higher robustness, with only a single failed case, but Fig. 3 shows that in the absence of loop closure, it tends to accumulate noticeable trajectory drift over long sequences.

### 4.3. Geometry Evaluation

We report point-cloud evaluation results on Waymo [28] and nuScenes [3] in Table 3 and Table 4. To avoid VGGT-SLAM [18]’s divergent predictions from dominating the metrics, we clamp per-point errors to 10 m. It can be seen that our TALO achieves the best accuracy, completeness, and Chamfer Distance across most scenes and foundation models. However, it is important to note that the ground-truth point clouds are obtained by accumulating LiDAR sweeps, whose capture range and coverage differ significantly from cameras. As a result, these metrics do not reliably reflect true geometric accuracy. For example, in the two scenes visualized in Fig. 3, the reconstruction produced by VGGT-Long [5] exhibits clear trajectory drift, which in

Table 5. **Monocular camera** trajectory accuracy on **Waymo** [28], reported as ATE (RMSE [m]). Best results are **bold underlined**.

Method	16345.	18382.	31561.	34618.	40584.	52001.	61045.	Avg.
DROID-SLAM [32]	3.71	0.30	0.45	8.65	7.62	4.17	0.26	3.59
MAS3R-SLAM [22]	4.50	0.56	1.83	12.54	1.41	5.43	1.20	3.92
CUT3R [39]	8.78	3.81	5.79	24.02	7.26	13.21	3.23	9.44
VGGT-Long [5]	1.65	0.22	0.37	<b>3.62</b>	1.08	1.85	<b>0.10</b>	1.27
TALO	<b>0.71</b>	<b>0.19</b>	<b>0.22</b>	3.74	<b>0.87</b>	<b>1.63</b>	0.20	<b>1.08</b>

Table 6. **Monocular geometry** evaluation on **Waymo** [28], reported as Chamfer Distance. Best results are **bold underlined**.

Method	16345.	18382.	31561.	34618.	40584.	52001.	61045.	Avg.
DROID-SLAM [32]	2.70	5.69	3.89	5.53	5.84	TL	7.44	5.18
MAS3R-SLAM [22]	2.45	3.14	2.92	3.84	2.03	5.42	4.60	3.49
CUT3R [39]	5.92	5.25	5.58	6.13	3.87	7.31	5.37	5.63
VGGT-Long [5]	1.57	2.23	2.46	2.10	1.85	<b>1.80</b>	1.69	<b>1.96</b>
TALO	<b>1.53</b>	<b>2.17</b>	<b>2.43</b>	<b>2.03</b>	<b>1.80</b>	2.14	<b>1.63</b>	<b>1.96</b>

turn warps the predicted geometry. Yet because LiDAR covers a much larger spatial extent than image-based predictions, the warped point clouds still lie largely within the LiDAR coverage region. Consequently, VGGT-Long may obtain similar or even lower error scores despite producing visibly distorted geometry. Furthermore, we additionally include zoomed-in views in Fig. 3. These close-ups show that our method recovers sharper and more accurate fine-grained geometry, largely eliminating multi-layer artifacts which are frequently observed in prior methods (e.g., ghosted façades and duplicated vehicles) caused by misaligned submaps. This improvement arises from our globally aggregated control points and the ability of TPS to correct spatially varying distortions while preserving global smoothness and local rigidity.

### 4.4. Ablation Study

To further understand the behavior of our system, we conduct several ablations on Waymo [28] using VGGT [38].

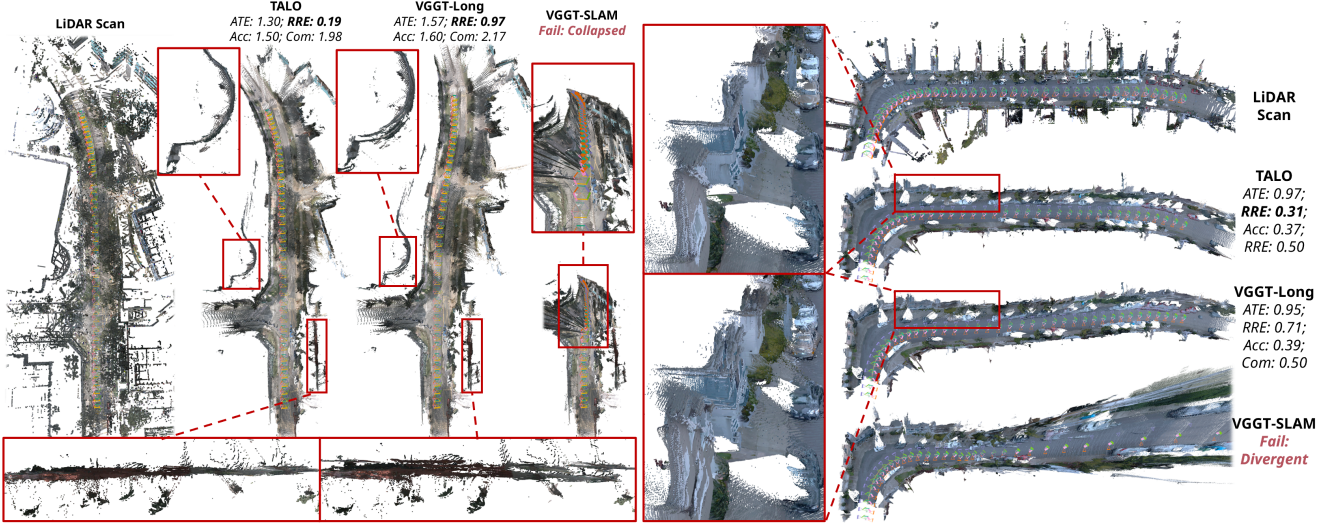


Figure 3. Qualitative comparison of the reconstructed trajectories and geometries with  $\pi^3$  [42] as backbone on **nuScenes** [3] scene-0039 (left) and **Waymo** [28] scene 16345319168590318167 (right), respectively. More results are shown in the supplementary materials.

In addition to the surround-view setting, we also evaluate a monocular configuration using only the front camera. We compare TALO with a classic SLAM pipeline, DROID-SLAM [32], as well as two online DUST3R-like reconstruction methods, CUT3R [39] and MAST3R-SLAM [22]. Trajectory and geometry results are reported in Table 5 and Table 6, respectively. It can be seen that TALO achieves the best camera trajectory accuracy and reconstruction quality across nearly all scenes.

We further analyze the effects of camera count and submap size; results are summarized in Fig. 4. Both VGGT-Long [5] (Sim(3)) and our method remain relatively stable under varying camera numbers and submap sizes, exhibiting consistent trends: (1) larger submaps yield lower trajectory error, and (2) more cameras improve geometric accuracy. This is likely because foundation models benefit from increased viewpoint diversity, producing more stable and accurate predictions. Importantly, our method outperforms VGGT-Long under all tested configurations. For VGGT-SLAM [18] (SL(4)), we observe that trajectory and geometry errors generally decrease as both the number of cameras and the submap size increase. This is likely because richer viewpoints reduce noise in the foundation model’s geometry predictions, making the SL(4) estimation more stable and reducing the probability of catastrophic divergence.

## 5. Conclusion

We revisited online reconstruction with 3D vision foundation models and showed that global-warp alignment cannot correct the spatially varying geometric errors common in outdoor, multi-camera settings. We introduced TALO, a higher-DOF and long-term alignment framework that propagates sparse control points, fuses multi-view evidence into

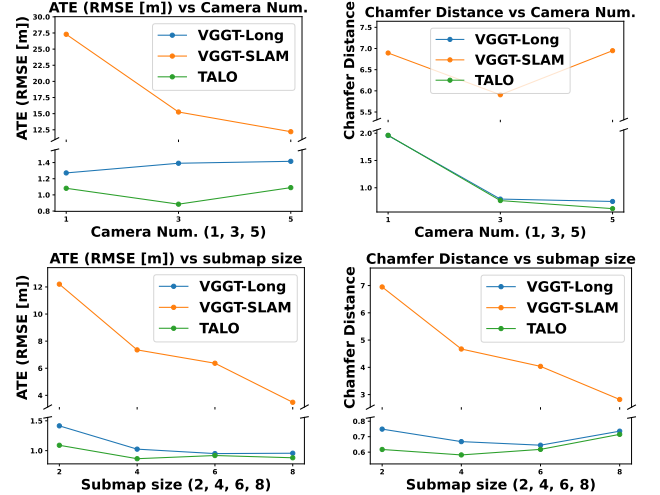


Figure 4. **Effect of camera count and submap size on trajectory and geometry accuracy.** Across all settings, TALO consistently achieves the lowest ATE and Chamfer Distance. Larger submaps reduce trajectory error, while additional cameras improve geometric stability, confirming that richer viewpoints strengthen VFM-based estimation.

canonical positions, and applies thin-plate deformation for spatially adaptive yet locally rigid correction. With a point-agnostic registration strategy robust to noisy predictions, TALO works as a plug-and-play module across models, datasets, and camera setups, yielding consistent gains on nuScenes and Waymo for both monocular and surround-view inputs. Future directions include uncertainty-aware control-point propagation, hierarchical deformation models for large-scale outdoor scenes, tighter coupling with video-native 3DVFM, and more principled treatment of fast motion and challenging viewpoints.



## References

- [1] F.L. Bookstein. Principal warps: thin-plate splines and the decomposition of deformations. *IEEE TPAMI*, 11(6):567–585, 1989. 2, 5
- [2] Yohann Cabon, Lucas Stofl, Leonid Antsfeld, Gabriela Csurka, Boris Chidlovskii, Jerome Revaud, and Vincent Leroy. Must3r: Multi-view network for stereo 3d reconstruction. In *CVPR*, 2025. 3
- [3] Holger Caesar, Varun Bankiti, Alex H. Lang, Sourabh Vora, Venice Erin Liong, Qiang Xu, Anush Krishnan, Yu Pan, Giancarlo Baldan, and Oscar Beijbom. nuscenes: A multimodal dataset for autonomous driving. In *CVPR*, pages 11618–11628, 2020. 1, 6, 7, 8, 2, 3
- [4] Hainan Cui, Xiang Gao, Shuhan Shen, and Zhanyi Hu. Hsfm: Hybrid structure-from-motion. In *CVPR*, pages 2393–2402, 2017. 2
- [5] Kai Deng, Zexin Ti, Jiawei Xu, Jian Yang, and Jin Xie. Vggt-long: Chunk it, loop it, align it – pushing vggt’s limits on kilometer-scale long rgb sequences, 2025. 1, 2, 3, 6, 7, 8
- [6] Jean Duchon. Splines minimizing rotation-invariant seminorms in sobolev spaces. In *Constructive theory of functions of several variables: proceedings of a conference held at oberwolfach April 25–May 1, 1976*, pages 85–100. Springer, 2006. 2, 5
- [7] Qiancheng Fu, Qingshan Xu, Yew-Soon Ong, and Wenbing Tao. Geo-neus: Geometry-consistent neural implicit surfaces learning for multi-view reconstruction. *NeurIPS*, 2022. 2
- [8] Yang Fu, Sifei Liu, Amey Kulkarni, Jan Kautz, Alexei A. Efros, and Xiaolong Wang. Colmap-free 3d gaussian splatting. In *CVPR*, pages 20796–20805, 2024. 3
- [9] Silvano Galliani, Katrin Lasinger, and Konrad Schindler. Massively parallel multiview stereopsis by surface normal diffusion. In *ICCV*, pages 873–881, 2015. 2
- [10] Richard Hartley, Jochen Trumpf, Yuchao Dai, and Hongdong Li. Rotation averaging. *IJCV*, 103(3):267–305, 2013. 4
- [11] Binbin Huang, Zehao Yu, Anpei Chen, Andreas Geiger, and Shenghua Gao. 2d gaussian splatting for geometrically accurate radiance fields. In *SIGGRAPH 2024 Conference Papers*. Association for Computing Machinery, 2024. 2
- [12] Nikhil Keetha, Norman Müller, Johannes Schönberger, Lorenzo Porzi, Yuchen Zhang, Tobias Fischer, Arno Knapitsch, Duncan Zauss, Ethan Weber, Nelson Antunes, Jonathon Luiten, Manuel Lopez-Antequera, Samuel Rota Bulò, Christian Richardt, Deva Ramanan, Sebastian Scherer, and Peter Kotschieder. Mapanything: Universal feed-forward metric 3d reconstruction, 2025. 1, 2, 3, 6, 7
- [13] Bernhard Kerbl, Georgios Kopanas, Thomas Leimkühler, and George Drettakis. 3d gaussian splatting for real-time radiance field rendering. *ACM TOG*, 42(4), 2023. 2
- [14] Yushi Lan, Yihang Luo, Fangzhou Hong, Shangchen Zhou, Honghua Chen, Zhaoyang Lyu, Shuai Yang, Bo Dai, Chen Change Loy, and Xingang Pan. Stream3r: Scalable sequential 3d reconstruction with causal transformer, 2025. 3
- [15] Vincent Leroy, Yohann Cabon, and Jerome Revaud. Grounding image matching in 3d with mast3r, 2024. 3
- [16] Shaohui Liu, Yidan Gao, Tianyi Zhang, Rémi Pautrat, Johannes L. Schönberger, Viktor Larsson, and Marc Pollefeys. Robust incremental structure-from-motion with hybrid features. In *ECCV*, 2024. 2
- [17] Yuzheng Liu, Siyan Dong, Shuzhe Wang, Yingda Yin, Yanchao Yang, Qingnan Fan, and Baoquan Chen. Slam3r: Real-time dense scene reconstruction from monocular rgb videos. *arXiv preprint arXiv:2412.09401*, 2024. 3
- [18] Dominic Maggio, Hyungtae Lim, and Luca Carlone. Vggt-slam: Dense rgb slam optimized on the sl (4) manifold. *arXiv preprint arXiv:2505.12549*, 2025. 1, 2, 3, 6, 7, 8
- [19] Ben Mildenhall, Pratul P. Srinivasan, Matthew Tancik, Jonathan T. Barron, Ravi Ramamoorthi, and Ren Ng. NeRF: Representing scenes as neural radiance fields for view synthesis. In *ECCV*, pages 405–421, 2020. 2
- [20] Pierre Moulon, Pascal Monasse, Romuald Perrot, and Renaud Marlet. OpenMVG: Open multiple view geometry. In *International Workshop on Reproducible Research in Pattern Recognition*, pages 60–74. Springer, 2016. 2
- [21] Thomas Müller, Alex Evans, Christoph Schied, and Alexander Keller. Instant neural graphics primitives with a multiresolution hash encoding. *ACM TOG*, (4), 2022. 2
- [22] Riku Murai, Eric Dexheimer, and Andrew J. Davison. MAST3R-SLAM: Real-time dense SLAM with 3D reconstruction priors. In *Proceedings of the IEEE/CVF Conference on Computer Vision and Pattern Recognition*, 2025. 7, 8
- [23] Paul-Edouard Sarlin, Daniel DeTone, Tomasz Malisiewicz, and Andrew Rabinovich. Superglue: Learning feature matching with graph neural networks. In *CVPR*, 2020. 3
- [24] Johannes Lutz Schönberger and Jan-Michael Frahm. Structure-from-motion revisited. In *CVPR*, 2016. 2
- [25] Johannes Lutz Schönberger, Enliang Zheng, Marc Pollefeys, and Jan-Michael Frahm. Pixelwise view selection for unstructured multi-view stereo. In *ECCV*, 2016. 2
- [26] Noah Snavely, Steven M. Seitz, and Richard Szeliski. *Photo tourism: exploring photo collections in 3D*. Association for Computing Machinery, 2023. 2
- [27] Jiaming Sun, Zehong Shen, Yuang Wang, Hujun Bao, and Xiaowei Zhou. LoFTR: Detector-free local feature matching with transformers. *CVPR*, 2021. 3
- [28] Pei Sun, Henrik Kretzschmar, Xerxes Dotiwalla, Aurelien Chouard, Vijaysai Patnaik, Paul Tsui, James Guo, Yin Zhou, Yuning Chai, Benjamin Caine, Vijay Vasudevan, Wei Han, Jiquan Ngiam, Hang Zhao, Aleksei Timofeev, Scott Ettinger, Maxim Krivokon, Amy Gao, Aditya Joshi, Yu Zhang, Jonathon Shlens, Zhifeng Chen, and Dragomir Anguelov. Scalability in perception for autonomous driving: Waymo open dataset. In *CVPR*, 2020. 1, 6, 7, 8, 2, 3
- [29] Matthew Tancik, Ethan Weber, Evonne Ng, Ruilong Li, Brent Yi, Justin Kerr, Terrance Wang, Alexander Kristoffersen, Jake Austin, Kamyar Salahi, Abhik Ahuja, David McAllister, and Angjoo Kanazawa. Nerfstudio: A modular framework for neural radiance field development. In *ACM SIGGRAPH 2023 Conference Proceedings*, 2023. 2
- [30] Chengzhou Tang and Ping Tan. Ba-net: Dense bundle adjustment network, 2019. 3

- [31] Zhenggang Tang, Yuchen Fan, Dilin Wang, Hongyu Xu, Rakesh Ranjan, Alexander Schwing, and Zhicheng Yan. Mv-dust3r+: Single-stage scene reconstruction from sparse views in 2 seconds. *arXiv preprint arXiv:2412.06974*, 2024. 3
- [32] Zachary Teed and Jia Deng. Droid-slam: deep visual slam for monocular, stereo, and rgb-d cameras. In *NeurIPS*, 2021. 7, 8
- [33] Shinji Umeyama. Least-squares estimation of transformation parameters between two point patterns. *IEEE TPAMI*, 13(4): 376–380, 2002. 6
- [34] Grace Wahba. *Spline models for observational data*. SIAM, 1990. 2, 5
- [35] Hengyi Wang and Lourdes Agapito. 3d reconstruction with spatial memory. *arXiv preprint arXiv:2408.16061*, 2024. 3
- [36] Jianyuan Wang, Yiran Zhong, Yuchao Dai, Stan Birchfield, Kaihao Zhang, Nikolai Smolyanskiy, and Hongdong Li. Deep two-view structure-from-motion revisited. In *CVPR*, pages 8953–8962, 2021. 3
- [37] Jianyuan Wang, Nikita Karaev, Christian Rupprecht, and David Novotny. Vggsfm: Visual geometry grounded deep structure from motion. In *CVPR*, pages 21686–21697, 2024. 3
- [38] Jianyuan Wang, Minghao Chen, Nikita Karaev, Andrea Vedaldi, Christian Rupprecht, and David Novotny. Vggt: Visual geometry grounded transformer. In *CVPR*, 2025. 1, 2, 3, 6, 7
- [39] Qianqian Wang, Yifei Zhang, Aleksander Holynski, Alexei A Efros, and Angjoo Kanazawa. Continuous 3d perception model with persistent state. *arXiv preprint arXiv:2501.12387*, 2025. 3, 7, 8
- [40] Shuzhe Wang, Vincent Leroy, Yohann Cabon, Boris Chidlovskii, and Jerome Revaud. Dust3r: Geometric 3d vision made easy. In *CVPR*, pages 20697–20709, 2024. 3
- [41] Yuesong Wang, Zhaojie Zeng, Tao Guan, Wei Yang, Zhuo Chen, Wenkai Liu, Luoyuan Xu, and Yawei Luo. Adaptive patch deformation for textureless-resilient multi-view stereo. In *CVPR*, pages 1621–1630, 2023. 2
- [42] Yifan Wang, Jianjun Zhou, Haoyi Zhu, Wenzheng Chang, Yang Zhou, Zizun Li, Junyi Chen, Jiangmiao Pang, Chunhua Shen, and Tong He.  $\pi^3$ : Scalable permutation-equivariant visual geometry learning, 2025. 1, 2, 3, 6, 7, 8
- [43] Xingkui Wei, Yinda Zhang, Zhuwen Li, Yanwei Fu, and Xiangyang Xue. Deepsfm: Structure from motion via deep bundle adjustment. In *ECCV*, 2020. 3
- [44] Simon N Wood. Thin plate regression splines. *Journal of the Royal Statistical Society Series B: Statistical Methodology*, 65(1):95–114, 2003. 2, 5
- [45] Jianing Yang, Alexander Sax, Kevin J. Liang, Mikael Henaff, Hao Tang, Ang Cao, Joyce Chai, Franziska Meier, and Matt Feiszli. Fast3r: Towards 3d reconstruction of 1000+ images in one forward pass. In *CVPR*, 2025. 3
- [46] Zehao Yu, Anpei Chen, Binbin Huang, Torsten Sattler, and Andreas Geiger. Mip-splatting: Alias-free 3d gaussian splatting. In *CVPR*, pages 19447–19456, 2024. 2
- [47] Fengyi Zhang, Yadan Luo, Tianjun Zhang, Lin Zhang, and Zi Huang. Gaussianforest: Hierarchical-hybrid 3d gaussian splatting for compressed scene modeling, 2024. 2
- [48] Junyi Zhang, Charles Herrmann, Junhwa Hur, Varun Jampani, Trevor Darrell, Forrester Cole, Deqing Sun, and Ming-Hsuan Yang. Monst3r: A simple approach for estimating geometry in the presence of motion. *arXiv preprint arxiv:2410.03825*, 2024. 3
- [49] Kai Zhang, Gernot Riegler, Noah Snaveley, and Vladlen Koltun. Nerf++: Analyzing and improving neural radiance fields. *arXiv:2010.07492*, 2020. 2
- [50] Tianjun Zhang, Lin Zhang, Fengyi Zhang, Shengjie Zhao, and Yicong Zhou. I-dacs: Always maintaining consistency between poses and the field for radiance field construction without pose prior. *IEEE TCSVT*, 35(3):2646–2661, 2025. 3
- [51] Dong Zhuo, Wenzhao Zheng, Jiahe Guo, Yuqi Wu, Jie Zhou, and Jiwen Lu. Streaming 4d visual geometry transformer. *arXiv preprint arXiv:2507.11539*, 2025. 3

# TALO: Pushing 3D Vision Foundation Models Towards Globally Consistent Online Reconstruction

## Supplementary Material

### 6. Linear Transformation Assumptions

This section analyzes the hidden assumptions behind adopting a linear transformation between two submaps: different predictions differ only by a global scale in depth (Sim(3)) and/or by intrinsics that can be corrected through a projective warp (SL(4)). Specifically, consider two camera reconstructions  $\{\tilde{\mathbf{u}}_1, \mathbf{K}_1, \mathbf{D}_1, \mathbf{T}_1\}$  and  $\{\tilde{\mathbf{u}}_2, \mathbf{K}_2, \mathbf{D}_2, \mathbf{T}_2\}$  observing the same scene, where  $\tilde{\mathbf{u}} = (u, v, 1)$  denotes homogeneous pixel coordinates,  $\mathbf{K}$  the intrinsics,  $\mathbf{D}$  the predicted depth, and  $\mathbf{T} = [\mathbf{R} \mid \mathbf{t}]$  the extrinsics. The 3D point  $\mathbf{P}$  can be obtained by back-projection:

$$\mathbf{P} = [\mathbf{R} \mid \mathbf{t}]^{-1}(\mathbf{D}(u, v) \mathbf{K}^{-1} \tilde{\mathbf{u}}). \quad (8)$$

Now, if we wish to solve for the transformation  $\mathbf{H}$  relating  $\mathbf{T}_1$  and  $\mathbf{T}_2$  through  $\mathbf{P}_1$  and  $\mathbf{P}_2$ , three typical cases arise:

- Case 1: Consistent intrinsics and scaled depths. If  $\mathbf{K}_1 = \mathbf{K}_2$  and  $\mathbf{D}_2(u, v) = s \mathbf{D}_1(u, v)$  for a global scalar  $s$ , then the two reconstructions differ only by a uniform scale. This simplifying assumption is implicitly adopted by VGGT-Long [5]. There exists a similarity transformation  $\mathbf{T} = [s \mathbf{R} \mid \mathbf{t}] \in \text{Sim}(3)$  such that  $\mathbf{P}_2 = s \mathbf{R} \mathbf{P}_1 + \mathbf{t}$ , which perfectly aligns the two reconstructions.
- Case 2: Inconsistent intrinsics and scaled depths. When  $\mathbf{K}_1 \neq \mathbf{K}_2$  and  $\mathbf{D}_2(u, v) = s \mathbf{D}_1(u, v)$ , the change in intrinsics induces a global projective distortion that a single Sim(3) cannot capture. This assumption is adopted by VGGT-SLAM [18]. Nevertheless, under the projective reconstruction theorem, there always exists a homogeneous linear mapping  $\mathbf{H} \in \text{SL}(4)$  that transforms one reconstruction into the other such that  $\mathbf{P}_1 = \mathbf{H} \mathbf{P}_2$ .
- Case 3: Nonlinear depth distortion. When the depth predictions deviate nonlinearly across spatial locations, i.e.,  $\mathbf{D}_2(u, v) = f(\mathbf{D}_1(u, v))$ , where  $f(\cdot)$  is non-linear and spatially varying, no global linear transformation can exactly align the two reconstructions, regardless of whether the internal calibration is consistent. Any linear alignment forces the optimizer to overfit one region at the expense of another, and bend the trajectory to compensate for local depth inconsistencies.

This analysis exposes the hidden assumptions underlying the two point-based submap alignment methods and explains their fundamental limitations. The more severely the corresponding assumption is violated, the poorer the alignment performance becomes. In scenarios with large submap size and few inter-submap alignments, the violation is often mild and aligns more closely with Case 1 and Case 2, allowing VGGT-Long [5] and VGGT-SLAM [18] to perform

reasonably well. However, realistic outdoor multi-camera settings generally correspond to Case 3, where the assumptions in Case 1 and Case 2 rarely hold. As a result, enforcing a global rigid or projective transformation inevitably leaves residual inconsistencies and distorts the trajectory.

### 7. Additional Qualitative Comparisons

We provide additional qualitative comparisons in Fig. 5, 6, 7, and 8. As shown, VGGT-Long [5] (Sim(3)) exhibits noticeable trajectory drift in long-range sequences, together with local misalignments that manifest as multi-layer artifacts in the reconstructed geometry. VGGT-SLAM [18] (SL(4)) is often disrupted by noise in the predicted point clouds, leading to severe geometric divergence or complete reconstruction failure. In contrast, TALO produces trajectories that closely match the ground truth and yields locally well-aligned geometry with clean, artifact-free details.



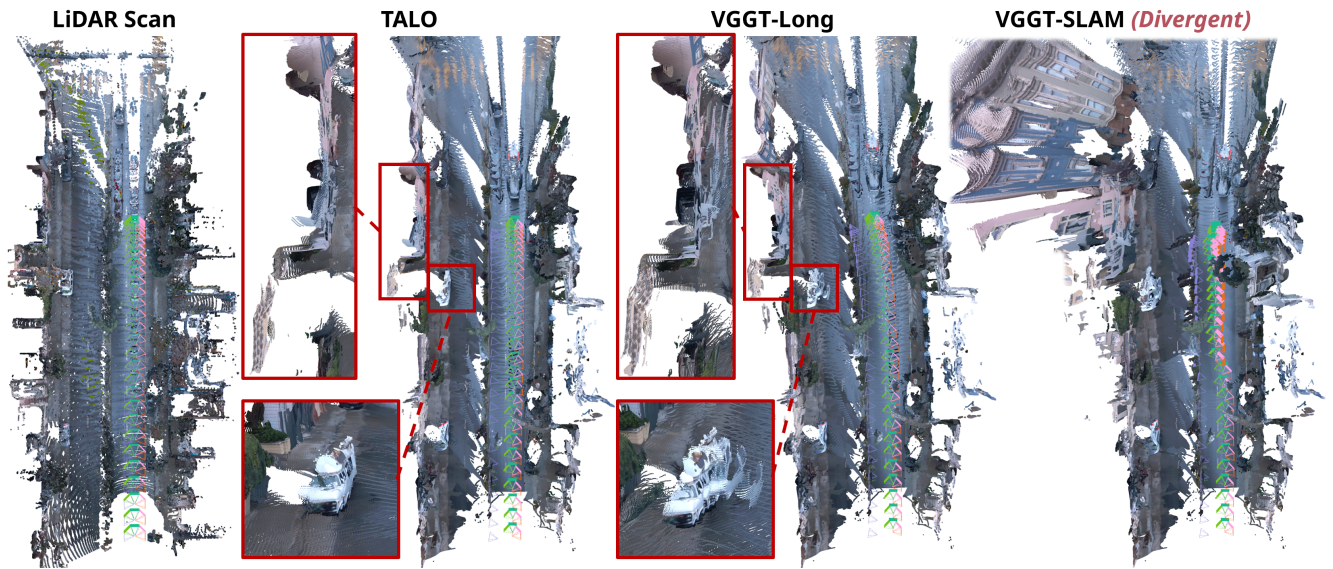


Figure 5. Qualitative comparison with VGGT [38] on Waymo [28] scene 6104545334635651714.

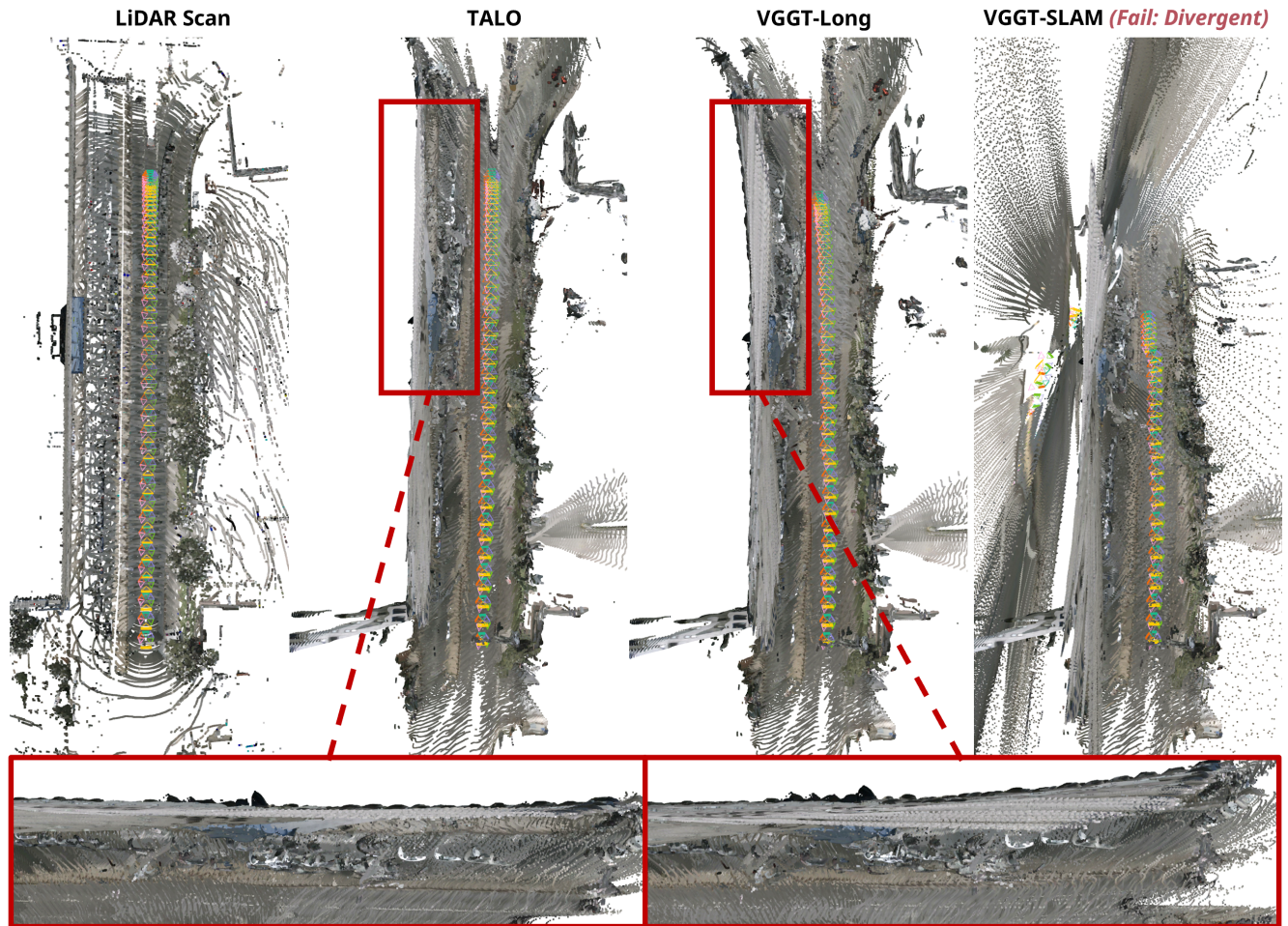


Figure 6. Qualitative comparison with VGGT [38] on nuScenes [3] scene-0094.



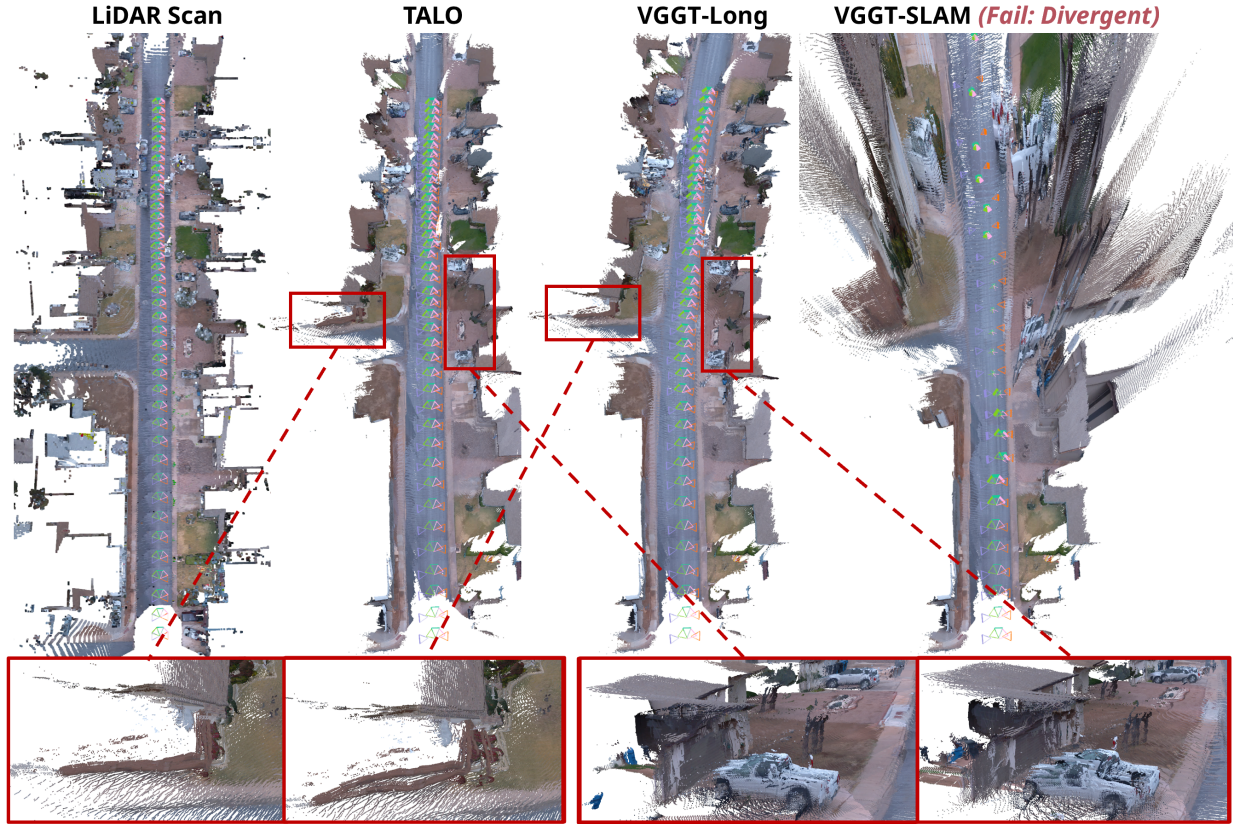


Figure 7. Qualitative comparison with  $\pi^3$  [42] on Waymo [28] scene 3156155872654629090.

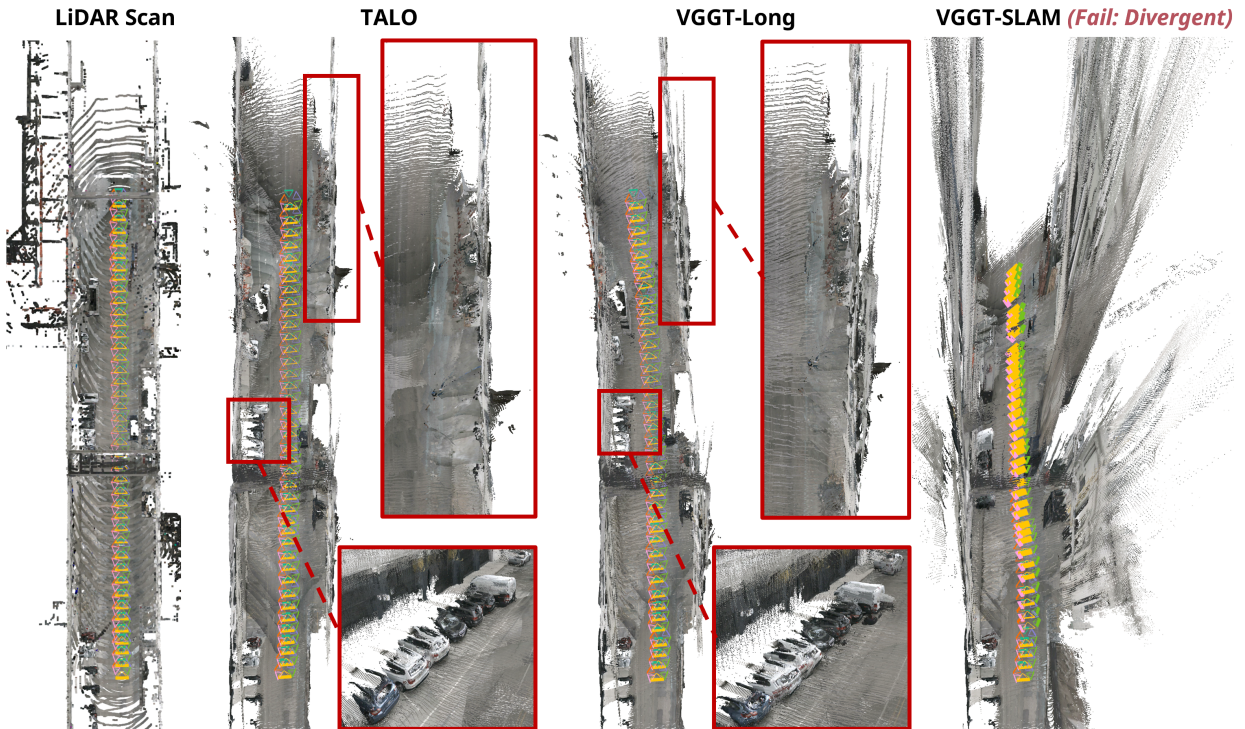


Figure 8. Qualitative comparison with  $\pi^3$  [42] on nuScenes [3] scene-0092.